



Cite this: DOI: 10.1039/d0tc04982d

Effect of thiophene/furan substitution on organic field effect transistor properties of arylthiadiazole based organic semiconductors†

Anna Pachariyangkun,^a Masayuki Suda,^b Sarinya Hadsadee,^c Siriporn Jungsuttiwong,^{ib} Phattananawee Nalaoh,^{ib} Pichaya Pattanasattayavong,^{ib} Taweesak Sudyoadsuk,^a Hiroshi M. Yamamoto^{*b} and Vinich Promarak^{ib} ^{*ad}

Four donor–acceptor (D–A) type organic semiconductors, consisting of 5-hexylthiophene with thiophene/furan flanked benzothiadiazole/naphthothiadiazole, were investigated for organic field effect transistor (OFET) application. Despite being an analogue of thiophene, furan has received less attention in organic electronics due to its dissimilar properties to thiophene and instability in photochemical oxidation. Nevertheless, this study determines that furan could display comparable charge transport properties to its analogue. The extension of the electron-accepting thiadiazole core with the benzo group and different heteroatom flanking groups were investigated to show that the performance of OFETs is dependent on the molecular orbital, geometry, and packing. Bottom-gate bottom-contact device configuration was used to study the OFET transport properties of all the molecules. We successfully proved that a furan unit is a promising building block with a mobility (μ_{\max}) of $0.0122 \text{ cm}^2 \text{ V}^{-1} \text{ s}^{-1}$ for devices employing furan-substituted benzothiadiazole as the channel layer.

Received 21st October 2020,
Accepted 5th November 2020

DOI: 10.1039/d0tc04982d

rsc.li/materials-c

Introduction

Organic semiconductors have emerged as a promising alternative to conventional inorganic semiconductors for their large area, low cost, and low temperature manufacturing techniques.¹ For over 20 years, organic semiconductors have received a lot of attention in the scientific community due to their potential applications in optoelectronic devices such as organic photovoltaics (OPVs), organic light emitting diodes (OLEDs), and organic field effect transistors (OFETs).² Development of organic semiconducting materials for field effect transistors (FETs) has been researched intensively due to their great potential in the field of “plastic electronics” in terms of possible low production cost,

light-weight/flexible substrates, and large area production.³ Over the past few years, research in OFETs has led to an understanding of the fundamental physics of charge transport in organic semiconductors where the field effect mobility has increased from values less than $10^{-4} \text{ cm}^2 \text{ V}^{-1} \text{ s}^{-1}$ to values exceeding $10 \text{ cm}^2 \text{ V}^{-1} \text{ s}^{-1}$.⁴ Improvements in organic semiconductor performances have promoted OFETs to be used in various applications such as flexible displays, e-paper, and radio frequency identification tags (RFID).⁵

Organic semiconductors could be categorized into two main classes: polymers and small molecules. With longer conjugation lengths and excellent film forming capabilities, organic polymers are remarkably compatible with large area applications.⁶ However, organic polymers suffer from the broad range distributions of molecular weight, consequently leading to variations in device performances. On the other hand, small organic molecules retain their high degree of order, high functionalization, and well-defined structures resulting in lower batch variations.⁷ Advancement of designs in organic semiconductor molecules with high π -orbital planarity and excellent inter- and intramolecular charge carrier transport could lead to the realization of high performance OFETs as the molecular structure and packing have a direct impact on the FET performances.⁸ Donor–acceptor (D–A) compositions have been commonly applied to design systems as it is an applicable approach to take advantage of the intermolecular D–A interaction favouring close co-facial D–A π -stacking.⁹

^a Department of Materials Science and Engineering, School of Molecular Science and Engineering, Vidyasirimedhi Institute of Science and Technology, Wangchan, Rayong 21210, Thailand. E-mail: vinich.p@vistec.ac.th

^b Institute for Molecular Science, Myodaiji, Okazaki 444-8585, Japan. E-mail: yhiroshi@ims.ac.jp

^c Department of Chemistry and Center of Excellence for Innovation in Chemistry, Faculty of Science, Ubon Ratchathani University, Warinchumrap, Ubon Ratchathani 34190, Thailand

^d Research Network of NANOTEC-VISTEC on Nanotechnology for Energy, Vidyasirimedhi Institute of Science and Technology, Wangchan, Rayong 21210, Thailand

† Electronic supplementary information (ESI) available. CCDC 1972793 and 1971452. For ESI and crystallographic data in CIF or other electronic format see DOI: 10.1039/d0tc04982d

D–A conjugation is also known to finely tune the frontier molecular orbital energy levels, which allows better carrier injection and band gap properties.¹⁰ Although a lot of studies have investigated the effect of single heteroatom replacement in OFETs, the structure–property relationships are still not well understood.¹¹ Many of the semiconductors utilized in reported OFETs are based on thiophene donor units and their derivatives.¹² In contrast, other five-membered aromatic rings such as furan have been inadequately examined for this application. Furan, discovered in 1870,¹³ has recently turned out to be a promising building block for organic semiconductors with its smaller size and high planarity, which may overcome its inferior aromaticity and smaller polarizability against thiophene.¹⁴ In addition, unlike most other building blocks, furan can be acquired from renewable resources, and various furan-based materials are biodegradable.¹⁵ In recent times, interest in utilizing furan based organic semiconductors has been expanding for organic electronic devices.¹⁶ Various D–A polymers based on furan units have been investigated for OFET applications.¹⁷ Nevertheless, only a few small molecules based on furan units have been reported, which signifies that the structure–property relationships of furan based small molecules still need further study. As far as we know, the reported furan based small molecules exhibit a mobility in the range of 10^{-6} – 10^{-2} $\text{cm}^2 \text{V}^{-1} \text{s}^{-1}$.¹⁸ In this study, we aim to understand more furan based small molecules and comprehend their structure–property relationships. Our intention is to investigate small molecules with different flanking donor groups and conjugated acceptor cores to understand their impact on OFET performances, by modifying the small molecule reported by P. Sonar,¹⁹ where all the target molecules are achieved *via* three-step synthesis. Therefore, we have chosen thiophene (T) and furan (F) for flanking groups along with naphthothiadiazole (NT) and benzothiadiazole (BT) for the conjugated core, while the flanking groups are end-capped with 5-hexylthiophene. The molecules are named as **T-NT-T**, **F-NT-F**, **T-BT-T**, and **F-BT-F** as shown in Fig. 1. In this paper, we have synthesized, characterized, and systematically investigated all the molecules for OFET application. All the molecules showed similar electronic properties upon substituting thiophene with a furan spacer unit, while the geometrical structures were strongly influenced by the substitution. In particular, the planarity of the molecules could be greatly enhanced by the addition of furan units. Moreover, we have found out that the furan units could lower the melting temperature of the

compounds compared to the thiophene analogue. We have demonstrated that a furan unit is a useful building block for organic semiconductors where it can outperform its analogue when incorporated with appropriate design.

Results

Synthesis

The synthesis route towards the four target molecules is depicted in Scheme S1 (ESI[†]). Firstly, **BT-di-Br** and **NT-di-Br** cores and 2-furyl-boronic acid and/or 2-thiophene-boronic acid were coupled together by the Suzuki–Miyaura cross-coupling reaction with $\text{Pd}(\text{PPh}_3)_4$ as a catalyst and Na_2CO_3 as a base to produce compounds **1**, **2**, **3**, and **4**. The resulting compounds were then brominated at the 2-thiophene or 2-furan position using *N*-bromosuccinimide (NBS) as the bromine source to obtain compounds **5**, **6**, **7**, and **8**, respectively. Lastly, the brominated compounds were subjected to coupling with 5-hexylthiophene-boronic acid to afford the target molecules in high yields. The target molecules were purified by column chromatography and were readily soluble in common organic solvents at room temperature. Structure confirmation was done by nuclear magnetic resonance (NMR), matrix-assisted laser desorption/ionization-time of flight (MALDI-TOF), and Fourier transform infrared spectroscopy (FTIR) (Fig. S1–S6, ESI[†]).

Theoretical calculations

To gain insights into the electronic and geometrical structures of the molecules, the optimized ground-state structures of the compounds were calculated by density functional theory (DFT) at the B3LYP/6-311G(d,p) level as shown in Fig. 2 and Table 1.

It can be observed that molecules having the BT core provided a co-planar structure in **F-BT-F** and **T-BT-T** which can enhance the co-facial π -stacking from the donor to acceptor moiety. On the other hand, **F-NT-F** and **T-NT-T** having NT as the core, with an extended benzo group, exhibited a more twisted dihedral angle compared to those with the BT core due to steric repulsion. It is notable that furan-containing molecules exhibit smaller dihedral angles than their thiophene analogues. The backbone twists are anticipated to inhibit strong π - π interactions and compact and ordered packing that are generally correlated with favourable charge transport properties.²⁰ This means that furan may have better ability to form efficient intermolecular interaction for electrical transport, if the stacking mode of these molecules is the same.

From the distribution of the highest occupied molecular orbital (HOMO) and the lowest unoccupied molecular orbital (LUMO) of the investigated structures (Fig. 3), it was illustrated that the electron density of the HOMOs is delocalized on the donor, whilst that of the LUMOs is concentrated on the acceptor of the molecules. This shows the ability of furan to conjugate with both the donor and acceptor moieties in the HOMO. It is notable that the LUMO+1 orbitals also show good D–A conjugation. The calculated HOMO and LUMO energy levels, along with the energy band gap (E_g), are depicted in

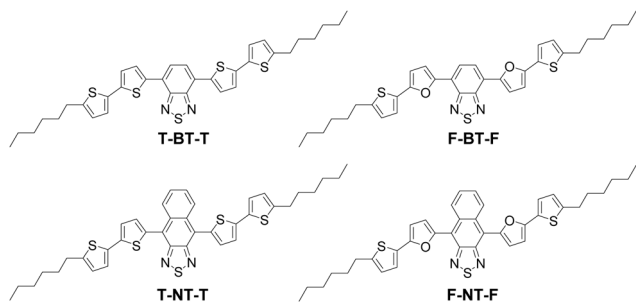


Fig. 1 Molecular structures of arylthiadiazole based organic semiconductors.

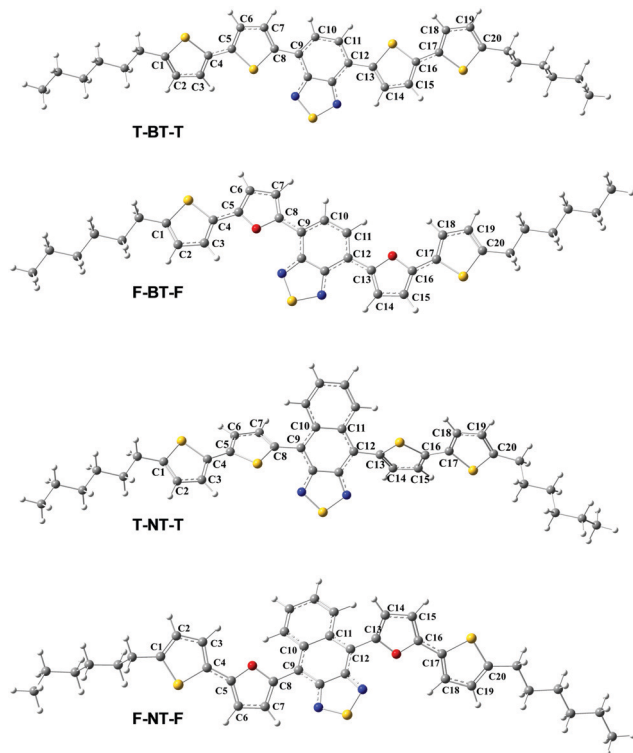


Fig. 2 Optimized structures calculated using the B3LYP/6-311G(d,p) level of theory.

Table 1 Dihedral angles of the optimized structures in dichloromethane solution

Dihedral angles ^a (°)	F-BT-F	T-BT-T	F-NT-F	T-NT-T
C3–C4–C5–C6 (D–D)	2.67	17.81	1.55	22.13
C7–C8–C9–C10 (D–A)	12.50	8.33	28.07	49.82
C11–C12–C13–C14 (A–D)	0.71	9.62	44.53	50.3
C15–C16–C17–C18 (D–D)	0.41	17.84	2.77	20.46

^a Calculated at B3LYP/6-311G(d,p) level of theory.

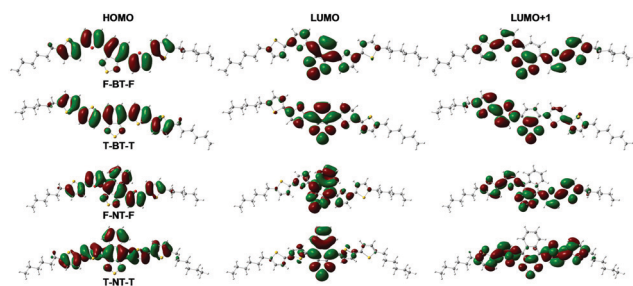


Fig. 3 Distributions of the HOMO, LUMO, and LUMO+1 calculated at B3LYP/6-311G(d,p) level of theory.

Fig. 4a. The HOMO levels of the furan-containing molecules are always higher than those of the thiophene analogues, reflecting higher furan HOMO levels than those of thiophene. The E_g of **T-BT-T** is the largest (2.27 eV) followed by **F-BT-F** (2.25 eV), **T-NT-T** (2.22 eV), and **F-NT-F** (1.95 eV) with the smallest E_g value. Compounds having the NT core exhibited a lower LUMO

level which could be attributed to the stronger electron accepting properties that originate in the extended benzo group which allows the electron to better delocalize along the backbone. Furthermore, absorption spectra of all the molecules were calculated by using TD-CAM-B3LYP/6-311G(d,p) level of theory (Fig. 4b). The effects of solvation using dichloromethane were observed using the C-PCM solvation model. Table 2 displays the excitation energies, electronic transition, oscillator strengths and absorption wavelengths for all the compounds. As seen from the photophysical calculations, the absorption profiles of the compounds exhibited two major regions at around 200–400 nm and 450–800 nm. The absorption in the range of 300–400 nm can be assigned to the π - π^* transition, while the range of 450–800 nm is associated with intramolecular charge transfer (ICT) processes. By observing the absorption range, compounds containing NT showed a bathochromic shift in the absorption maxima compared to the BT core compounds.

To examine intramolecular charge separation, the charge transfer parameter was analysed. Charge transfer (CT) is very important for analysis of the mechanism of optical/dielectric properties. The charge density difference is a method used to analyse the transition corresponding to the CT excited state. We calculated the charge density differences (Δq) between the ground and excited states. Upon analysis of the amount of transferred charge, **T-NT-T** showed the largest amount of electron transfer between the ground and first excited states (Table 2). It is evident that significant charge density differences are observed between the acceptor and donor groups. As shown in Fig. 4c, the blue region represents the negative charge density (electron gain), while the red region represents the positive charge density (electron loss), indicating the movement of electron density inside the molecule upon excitation. The charge transfer distances (d^{CT}) of the compounds were calculated where **F-BT-F** shows the largest value followed by **T-BT-T**, **T-NT-T**, and **F-NT-F** (Table 2). No significant difference was observed between furan and thiophene.

Ionization potential (IP) and electron affinity (EA) were investigated to understand the carrier injection abilities of the compounds. EA and IP would lead to electron and hole transport, respectively. For both p-type and n-type OFETs, the electrode materials should have work functions suitable for injection of holes/electrons into the HOMO/LUMO of the semiconductor materials. Previous calculations by Y. Zhang and co-workers showed that molecular compounds with large vertical electron affinity (VEA) will show advantage as n-type organic semiconductors in terms of charge injection, while those with small vertical ionization potential (VIP) are favorable as p-type semiconductors.²¹ Thus, the VEA and VIP values of the compounds were calculated at the B3LYP/6-311G(d,p) level (Table 2). For the Au electrode, the key to the efficient injection of charge carrier is that the VIP values should be close to the Au work function (5.1 eV). The VEA values suitable for electron transport materials need to be at least 3.0 eV but should not be greater than 5.0 eV. From the calculation, it can be observed that the VIP values of all the molecules are close to the Au work function. On changing the BT core to the NT core, the VEA values of the compounds

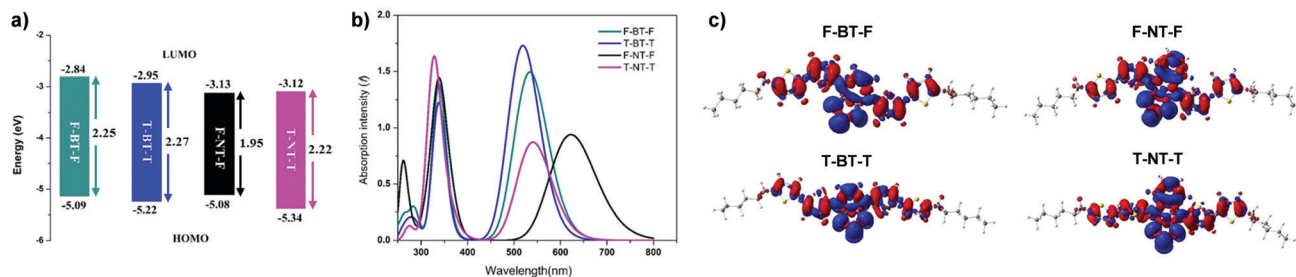


Fig. 4 (a) Calculated energy gap (E_g) between the HOMO and LUMO of arythiadiazole based organic semiconductors. (b) Calculated UV-vis absorption spectra in CH_2Cl_2 solution at the TD-CAM-B3LYP/6-311G(d,p) level. (c) Computed charge density difference (Δq) between the ground state to the S_1 excited states with an isosurface value of 0.0005 a.u. Blue: $\Delta q < 0$ (electron increase); red: $\Delta q > 0$ (electron decrease).

Table 2 Theoretical calculation data of arythiadiazole based organic semiconductors

Compound	λ_{abs} (nm) in CH_2Cl_2^a	f^{ab}	Transition ^a	Δq^c ($ e^- $)	$d^{\text{CT}d}$ (Å)	VEA ^e	VIP ^e
F-BT-F	338	1.0480	HOMO → LUMO+1	0.635	1.37	2.86	5.07
	533	1.1345	HOMO → LUMO				
T-BT-T	337	0.9238	HOMO → LUMO+1	0.615	1.29	2.96	5.20
	518	1.3134	HOMO → LUMO				
F-NT-F	338	0.9090	HOMO → LUMO+1	0.600	0.90	3.14	5.05
	622	0.7135	HOMO → LUMO				
T-NT-T	330	0.9702	HOMO → LUMO+1	0.669	0.93	3.12	5.32
	540	0.6623	HOMO → LUMO				

^a Obtained using TD-CAM-B3LYP/6-311G(d,p). ^b Oscillator strength. ^c Charge density differences. ^d Charge-transfer distance. ^e Calculated at B3LYP/6-311G(d,p) level of theory.

have increased, and thus the possibility of electron injection from the gold electrode into the semiconductor increases.

Spectroscopic/thermal/structural data

The optical, electrochemical, thermal, and structural properties of the target molecules were investigated by UV-visible spectroscopy, cyclic voltammetry (CV), differential scanning calorimetry (DSC)/thermogravimetric analysis (TGA), and X-ray diffraction (XRD), respectively (Fig. 5). T-NT-T, F-NT-F, T-BT-T, and F-BT-F showed a π - π^* transition absorption maxima at 348 nm, 372 nm, 364 nm, and 352 nm and an ICT band at 547 nm, 615 nm, 516 nm, and 529 nm, respectively (Fig. 5a). The resulting experimental data were in the same trend of the calculated absorption as shown in Fig. 4b. This means no serious aggregation is formed in dichloromethane solution. CV was performed to calculate the HOMO and LUMO energy levels (Fig. 5b). The onset potentials of T-NT-T, F-NT-F, T-BT-T, and F-BT-F were observed and used to calculate the energies of the HOMO and LUMO levels of all the compounds reported in Table 3. This trend is also consistent with the calculated values, where NT has a lower LUMO level and furan/thiophene substitution does not change the HOMO level very much. Moreover, the HOMO energy levels calculated from CV are confirmed by photoelectron yield spectroscopy (AC-2) measurements.

The thermal properties of all small molecules were investigated by DSC and TGA under a nitrogen flow with a heating rate of $10\text{ }^\circ\text{C min}^{-1}$. The TGA thermogram (Fig. 5c) illustrates that

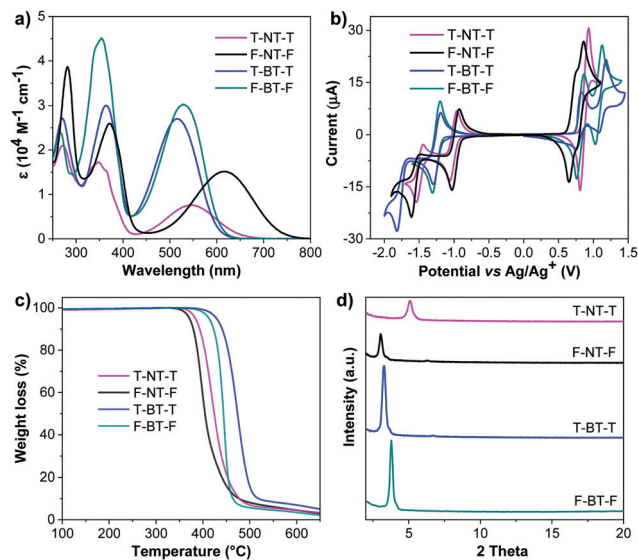


Fig. 5 (a) UV-vis absorption spectra in CH_2Cl_2 . (b) CV voltammogram measured in CH_2Cl_2 containing $n\text{-Bu}_4\text{NPF}_6$ as the supporting electrolyte at a scan rate of 50 mV s^{-1} under an Ar atmosphere. (c) TGA thermograms recorded at a heating rate of $10\text{ }^\circ\text{C min}^{-1}$ under a N_2 flow. (d) XRD patterns of the thin films on the SiO_2 substrate.

all small molecules exhibit good thermal stability and will not degrade during the device fabrication process. The thermal decomposition temperatures (T_d) were estimated to be 342, 359, 375, and 382 $^\circ\text{C}$ for F-NT-F, T-NT-T, F-BT-F, and T-BT-T, respectively. It is notable that the thermal stability of the furan substituted molecules is comparable to that of the thiophene analogues in TGA measurements. The DSC thermograms shown in Fig. 6 revealed that T-BT-T has several mesophases before reaching a melting temperature (T_m) of 225 $^\circ\text{C}$, while F-BT-F and T-NT-T have only one peak at 112 and 149 $^\circ\text{C}$, respectively. From DSC traces, it could be predicted that the T-BT-T compound might exhibit better FET properties owing to its several mesophases. Furan containing molecules possessed a lower T_m compared to their thiophene analogues due to the smaller molecular weight of oxygen and weaker heteroatom-heteroatom intermolecular interactions. In addition, the XRD patterns of the thermally evaporated thin films on the SiO_2 substrate were collected (Fig. 5d) with the primary diffraction peak at $2\theta = 5.09, 3.06, 3.28,$ and 3.79° for T-NT-T, F-NT-F,

Table 3 Key physical data of arylthiadiazole based organic semiconductors

Compounds	λ_{abs}^a (nm)	T_m/T_d^b ($^{\circ}\text{C}$)	$E_g^{\text{opt}c}$ (eV)	HOMO/LUMO ^d (eV)	HOMO/LUMO ^e (eV)	2 theta ^f ($^{\circ}$)	<i>d</i> -Spacing ^g
F-BT-F	352, 529	112/375	2.04	-5.13/-3.40	-5.11/-3.07	3.79	23.3
T-BT-T	364, 516	225/382	2.07	-5.13/-3.38	-5.20/-3.13	3.28	26.9
F-NT-F	372, 615	60/342	1.68	-5.06/-3.65	-4.79/-3.11	3.06	28.8
T-NT-T	348, 547	149/359	1.90	-5.18/-3.61	-5.33/-3.43	5.09	17.3

^a Measured in CH_2Cl_2 . ^b T_m : melting temperature; T_d : decomposition temperature; measured by DSC and TGA under a N_2 flow at a heating rate of $10\text{ }^{\circ}\text{C min}^{-1}$. ^c Estimated from the absorption onset: $E_g^{\text{opt}} = 1240/\lambda_{\text{onset}}$. ^d HOMO estimated from CV: $\text{HOMO} = -(4.44 + E_{\text{onset}}^{\text{ox}})$ and $\text{LUMO} = -(4.44 + E_{\text{onset}}^{\text{red}})$. ^e HOMO measured by AC-2 of the neat film and the LUMO = HOMO + E_g . ^f Measured from evaporated thin films on the SiO_2 substrate. ^g Calculated from Bragg's law.

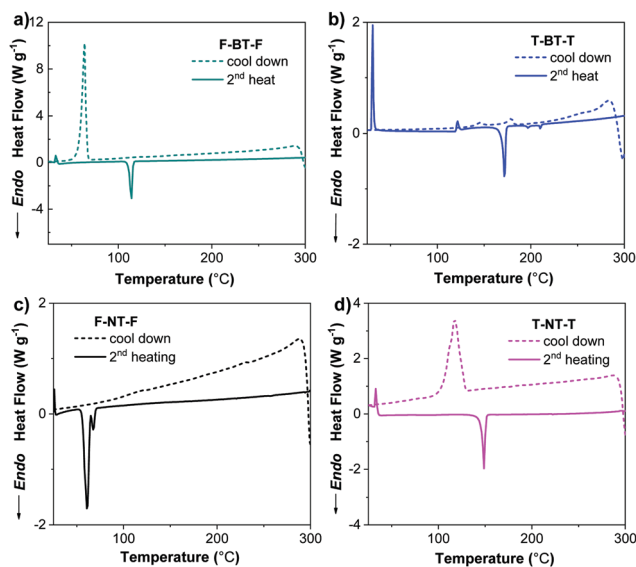


Fig. 6 DSC thermograms recorded at a heating rate of $10\text{ }^{\circ}\text{C min}^{-1}$ under a N_2 flow of (a) **F-BT-F**, (b) **T-BT-T**, (c) **F-NT-F**, and (d) **T-NT-T**.

T-BT-T, and **F-BT-F**, respectively, and the corresponding *d*-spacing is reported in Table 3.

The **F-NT-F** and **T-NT-T** single crystals were grown by solvent diffusion crystallization using dichloromethane and methanol to obtain needle like crystals. The crystal data, data collection, and structure refinement are reported in Table S1 (ESI[†]). **F-NT-F** and **T-NT-T** crystallize in the monoclinic $P2_1/n$ and triclinic $P\bar{1}$ space groups, respectively. The asymmetric units of the **F-NT-F** and **T-NT-T** single crystal data are shown in Fig. S7 and S8 (ESI[†]), respectively. From observing the single crystal structure, the thiophene unit in **T-NT-T** exhibited a higher twist in the torsional angle with the NT acceptor core compared to the furan unit in **F-NT-F** (Fig. 7a). The **F-NT-F** backbone structure can impose strong “conformational locks” which causes the planarity and rigidity of the side groups which is in accordance with the calculation of many reports on benzothiadiazole-cored oligomers with aryl flanking units.²² The furan ring adjacent to the NT core has two O–H (2.11–2.19 Å) and N–H (2.34–2.47 Å) bonds, while the thiophene ring did not exhibit any intramolecular interaction with the NT core but only short contacts with the adjacent thiophene rings (2.90–3.01 Å). This is in agreement with the calculation and the furan units may be beneficial in solid-state packing compared to the thiophene units. As mentioned previously, the high twist along the backbone of the

molecules, especially for **T-NT-T**, could restrict strong π - π interactions. The molecular dipole moments of the molecules in the crystal structures were calculated as shown in Fig. 7b. The dipole moment of both **F-NT-F** and **T-NT-T** is directed away from the electron deficient thiadiazole ring with an absolute dipole moment of 1.407 and 2.294 debye, respectively. Alignment of the dipole moment of the crystal structure showed that both **F-NT-F** and **T-NT-T** exhibited antiparallel packing (Fig. 7c), which is expected for organic small molecules. The stronger dipole-dipole interaction in **T-NT-T** could lead to higher thermal stability. To investigate the dimer interaction further, quantum resonance calculation was performed on the dimer of both **F-NT-F** and **T-NT-T** as shown in Fig. 7d. For **F-NT-F**, the ΔE between the HOMO–1 (bonding) and HOMO (anti-bonding) was 0.03 eV, indicating that there is some intermolecular interaction between the molecule and the next molecule *via* the thiophene to furan ring, respectively. On the other hand, ΔE between the HOMO–1 and HOMO of **T-NT-T** was found to be 0.00 eV which might indicate that there is no charge transfer between the dimer due to the non-planarity of the molecule.

OFET performances

Bottom-gate bottom-contact (BGBC) thin film transistors were fabricated to investigate the charge transport properties of the synthesized compounds. When using the bottom contact configuration, it is essential to consider the alignment of organic semiconductors on the electrodes. Small organic semiconductor molecules tend to align themselves by placing their electron clouds in the highest polarizable region.²³ Thus, when organic semiconductors are deposited on noble metals, like gold, which is inert and has no oxide on the surface, the molecules will tend to lay themselves in a different configuration compared to those on the dielectric layer. To reduce the carrier injection barrier and to improve the wettability, a self-assembled monolayer (SAM) was used to treat the electrode surface before depositing the small molecules.²⁴ 4-(Dimethylamino)benzenethiol (DABT) was used to create a covalent bond with the gold electrode prior to the organic semiconductor deposition. The dipole moment of this molecule will also modify the vacuum levels for the semiconductor. The small molecules were deposited by thermal evaporation with a thickness of 30 nm under a pressure of $\sim 10^{-5}$ Pa. The transfer curve and output characteristics are shown in Fig. 8 and the key parameters are reported in Table 4. The **T-BT-T** based device I (Fig. 8a and d) showed a maximum hole mobility (μ_{max}) of $1.37 \times 10^{-1} \text{ cm}^2 \text{ V}^{-1} \text{ s}^{-1}$, an on-off current ratio ($I_{\text{on}}/I_{\text{off}}$) of 8×10^5 , and a threshold voltage (V_{TH}) of

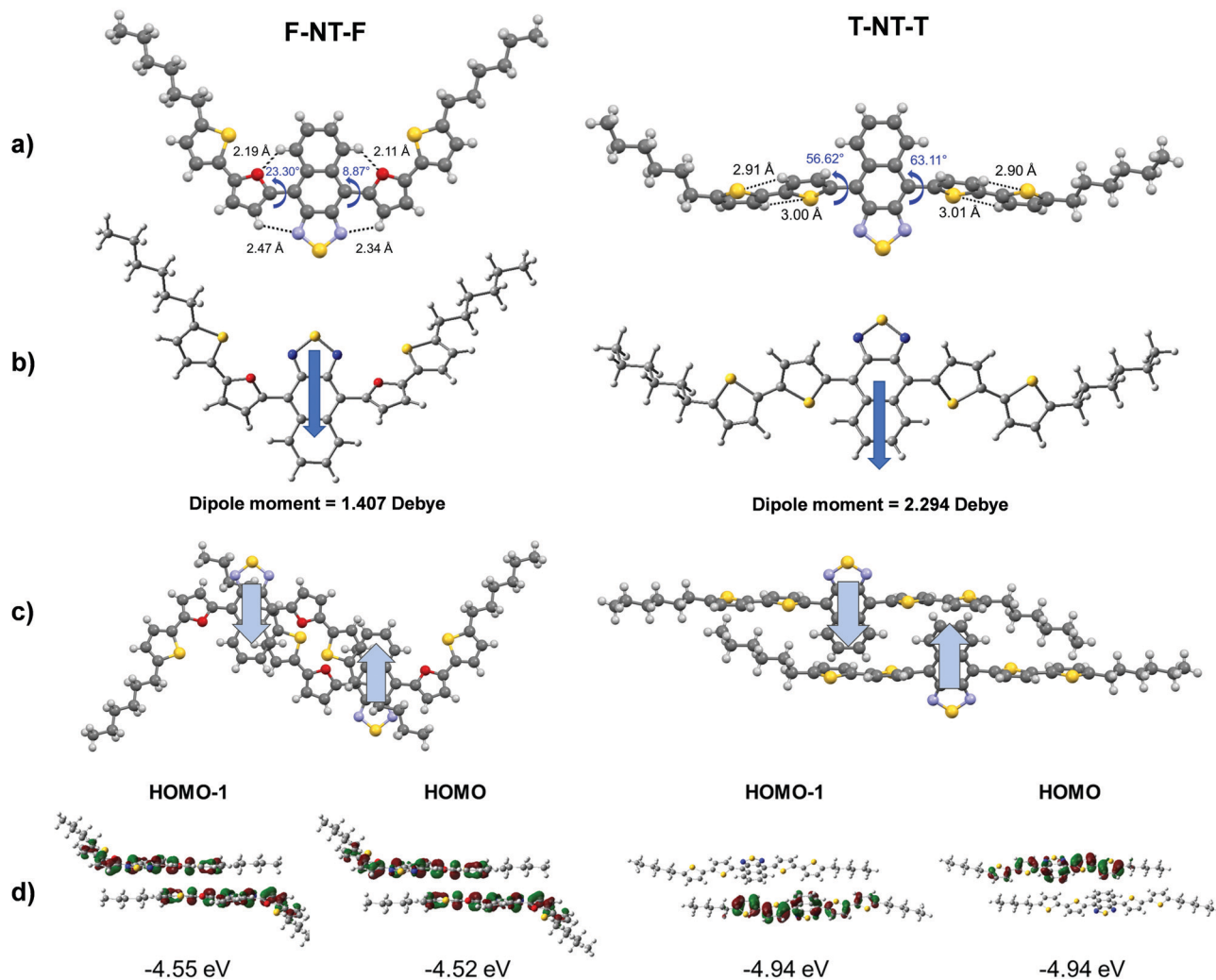


Fig. 7 (a) Crystal structure of **F-NT-F** and **T-NT-T**. (b) Calculated dipole moment of the crystal structures. (c) Alignment of the dipole moment of **F-NT-F** and **T-NT-T** in the π -stacking direction. (d) Calculation of HOMO-1 and HOMO of the dimer.

–10.9 V, whereas the **F-BT-F** based device II (Fig. 8b and e) and the **F-NT-F** based device III (Fig. 8c and f) showed an μ_{max} of 1.22×10^{-2} and $5.84 \times 10^{-3} \text{ cm}^2 \text{ V}^{-1} \text{ s}^{-1}$, a V_{TH} of –19.5 and –12.6, and an $I_{\text{on}}/I_{\text{off}}$ of 5×10^5 and 1×10^5 , respectively. Surprisingly, device IV, using **T-NT-T** as the channel layer, resulted in an inactive OFET performance. The devices of all the compounds were further investigated to study the effect of annealing with respect to the performance of the devices. The fabricated device was annealed at 100 °C for 1 hour in a vacuum oven prior to performance measurements. The transfer curve and mobility of the annealed devices are shown in Fig. S9 (ESI†). Annealing of the devices did not enhance the mobility as the performance of the devices was somewhat lower after annealing and the **T-NT-T** based device remained inactive. The reasons why the **T-NT-T** based device did not exhibit OFET properties could be attributed to the following explanations: (1) the low degree of backbone coplanarity of **T-NT-T** that was indicated by both quantum chemical calculations (Table 1) and the crystal structure (Fig. 7a) could constrain strong π - π interactions and (2) the small d -spacing (17.3 Å) of the **T-NT-T** molecule could be

correlated with the unit length in the b -axis (17.9 Å) of the crystal structure. The predicted alignment of the molecules is illustrated in Fig. 9a with the b -axis aligned along the d -spacing direction. In an ideal molecular alignment in OFETs, the π - π stacked building blocks should be aligned in the direction parallel to the current flow in the channel.²⁵ From observing the source to drain contact, it is seen that the direction of π - π interactions (red arrow) may constrict electron hopping from source to drain contact; (3) the VIP values of **T-NT-T** are not so close to the Au work function which could lead to difficult hole injection. The atomic force microscopy (AFM) images of the channel region (Fig. 9) showed that the substrates were completely covered with the semiconductor layer. **T-BT-T** and **F-BT-T** exhibited a well-organized morphology with crystalline nanograins, while **F-NT-F** had a larger granular texture which could be the consequence of recrystallization on the substrate due to the lower T_m of the molecule. The **T-NT-T** channel exhibited a fibrous grain although it did not exhibit OFET properties. In the case of **T-NT-T**, the molecular packing was not appropriate for electrical conduction, although the morphology of the channel layer was similar to that of the other compounds.

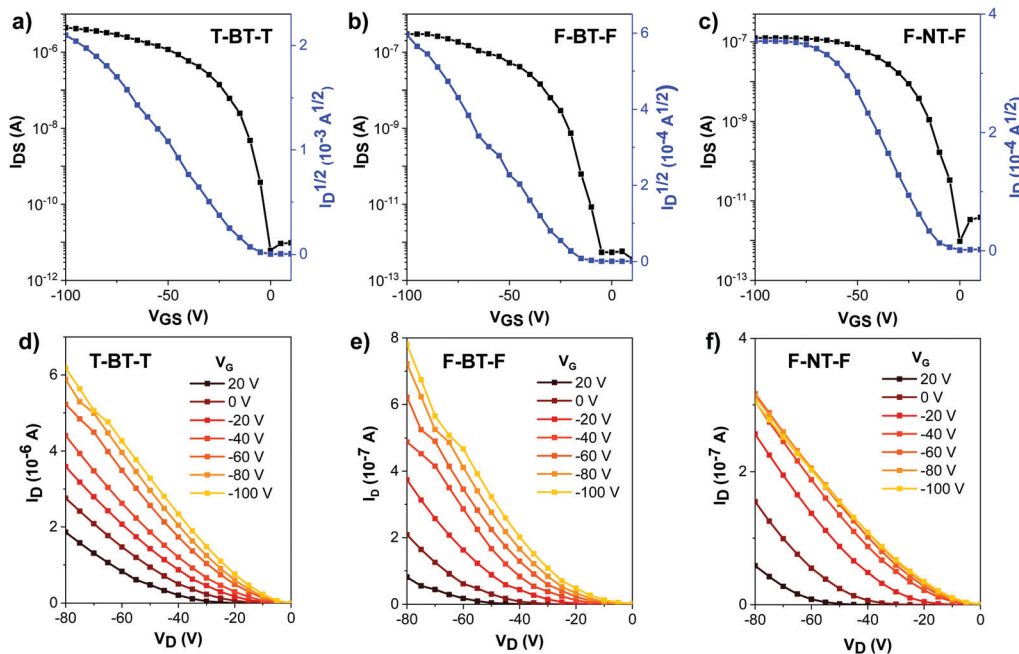


Fig. 8 (a) Transfer curves at $V_D = 50$ V of devices (a) I, (b) II, and (c) III. Output characteristics of devices (d) I, (e) II, and (f) III. Device dimension: channel length (L) = 100 μm ; channel width (W) = 100 μm .

Table 4 Summary of the OFET performance of arylthiadiazole derivatives

Device ^a	Channel	μ_{max} ($\text{cm}^2 \text{V}^{-1} \text{s}^{-1}$)	μ_{ave} ($\text{cm}^2 \text{V}^{-1} \text{s}^{-1}$)	V_{TH} (V)	$I_{\text{on}}/I_{\text{off}}$
I	T-BT-T	1.37×10^{-1}	1.29×10^{-1}	-10.9	8×10^5
II	F-BT-F	1.22×10^{-2}	9.87×10^{-3}	-19.5	5×10^5
III	F-NT-F	5.84×10^{-3}	5.78×10^{-3}	-12.6	1×10^5
IV	T-NT-T	N.A.	N.A.	N.A.	N.A.

^a Si/SiO₂/Ti-Au/arylthiadiazole derivatives (30 nm).

Discussion

We performed synthesis, calculation, characterization, and OFET measurements of four different D-A type small molecules. By comparing the calculation and spectroscopic data, we

confirmed that the frontier energy levels were consistent with the calculated results and proved that furan does not change the electronics properties very much when thiophene is replaced with it. Despite the above comparable electronic states between furan and thiophene, the preferred molecular orientation, which is correlated to the charge carrier properties, of the small molecules could be dissimilar. In the case of furan-containing molecules, the flatness of π conjugation becomes better than the thiophene analogue probably because the furan part is less bulky. According to the investigated calculation and single-crystal data, it could be predicted that the T-NT-T alignment in the thin films may obstruct the electrical current flow from the source to drain electrodes due to the high backbone twist, which agrees with the inactive OFET performance when employing T-NT-T as the

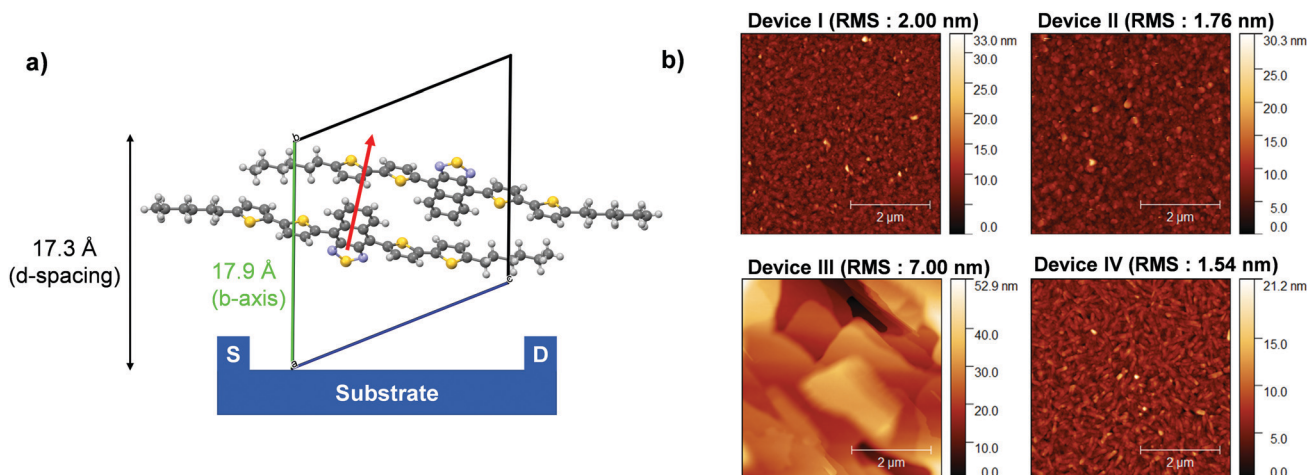


Fig. 9 (a) Proposed molecular alignment of T-NT-T. (b) AFM images of the channel layer in devices I–IV.

channel. On the other hand, **F-NT-F** showed smaller twist angles in the intramolecular dihedral angles and thus was able to form an aligned molecular packing that is suitable for the OFET channel. This conformational lock and compactness effect seem to be one of the benefits of the furan subunit as a semiconductor material. The best OFET performance was achieved by **T-BT-T** whose DSC data showed several mesophases in the heating process. The **F-BT-F** based device performance followed through although it did not show liquid crystalline nature, for which the reason is still unclear in our study and is left for future study. Significantly lower melting temperatures of the furan-based molecules may reflect weaker intermolecular interaction and lower dipole–dipole interactions which could benefit in low-temperature processing. Upon increasing the benzo group to the NT core, the furan containing compound (**F-NT-F**) is found to be superior to the thiophene containing compound (**T-NT-T**) thanks to the furan unit in enhancing the ordered molecular packing of the molecules. In summary, the incorporation of furan demonstrated comparable electronic levels and OFET performance to its analogue. More importantly, the molecular alignment of the molecules could have a direct impact on the OFET performance regardless of their similar energy levels.

Conclusions

In summary, we investigated four small molecules based on D–A conjugation for OFET application with regard to the incorporation of furan building blocks compared to its thiophene analogue. Through the D–A system approach, furan was proved to be an alternative backbone group to thiophene, although the thermodynamic properties such as melting point and liquid crystalline nature were different. The lowering of melting point by furan substitution seems to be effective when a given molecule exhibits too strong intermolecular interaction for low-temperature processing, for example. Based on the OFET performances, we have shown that furan units, with their availability in natural resources, can be used as potential building blocks for organic semiconductors. In addition, with the smaller atomic size of oxygen and higher planarity, utilizing furan units along with other appropriate building blocks could further tune the electronic/geometrical structures along with the physical properties and benefit the electric conduction in the solid state, thus improving the performances in organic electronic applications.

Experimental

Materials and methods

All reagents were purchased from Aldrich, Acros, or Tokyo Chemical Industry and used as received. NMR spectra were recorded on a Bruker Avance III HD 600 MHz spectrometer. UV-vis spectra were recorded as a dilute solution in a spectroscopic grade dichloromethane on a PerkinElmer Lambda 1050 spectrometer. CV measurements were carried out under an inert argon atmosphere with an Autolab potentiostat PGSTAT 101 device using a platinum counter electrode, a glassy carbon working electrode,

and an Ag/AgCl reference electrode in distilled CH₂Cl₂ with tetra-*n*-butylammonium hexafluorophosphate (*n*-Bu₄NPF₆) as the supporting electrolyte at a scan rate of 50 mV s⁻¹. Photoelectron spectroscopy (AC-2) was performed using a Riken-Keiki ultraviolet photoelectron spectrometer AC-2 in air. Morphologies of the channel layer were investigated using a Park Systems NX-10 AFM microscope using true non-contact mode and an NCHR cantilever. A Bruker microflex MALDI-TOF spectrometer was used to record high resolution mass spectra. DSC was operated using the Mettler Toledo model DSC823e at a heating rate of 10 °C min⁻¹ under a nitrogen flow. TGA was performed using a Rigaku model Thermoplus TG8120 analyzer at a heating rate of 10 °C min⁻¹ under a nitrogen flow. XRD thin films were measured using a Bruker D8 Advance diffractometer. FTIR was performed using a PerkinElmer Frontier FT-IR spectrometer. Single crystal-XRD crystallographic data was recorded using a Bruker D8 Venture diffractometer. APEX 3 software was used for collecting frames of data. OLEX 2 software was used for refinement, space group determination and solving the crystal structure. The intermolecular forces were analysed using the Platon program and the graphics of the crystal structures were produced using Mercury 4.2.²⁶ Structure CCDC deposition number of **F-NT-F**: 1972793 and **T-NT-T**: 1971452.† All quantum calculations were performed using the Gaussian 09 program by density functional theory.²⁷ The HOMO and LUMO distributions of the compounds were calculated at B3LYP/6-311G(d,p) level of theory. The UV-vis absorption spectra were calculated at TD-CAM-B3LYP/6-311G(d,p) level of theory.

Device fabrication and performance measurements

The device was fabricated using bottom-gate bottom-contact configuration with silicon, SiO₂ (350 nm), and Ti (2 nm)–Au (20 nm) as the gate, dielectric layer, and electrode, respectively. The electrode deposition was patterned by mask-less photolithography followed by metal sputtering with gaps of 5 μm, 10 μm, 30 μm, 50 μm, 100 μm, 150 μm, and 200 μm. The pre-patterned substrates were rinsed twice using acetone and once using isopropanol, and then subsequently dried with argon gas. They were then treated with UV–ozone plasma for 5 minutes prior to immersing in DABT solution for 2 h. Then the treated substrate was transferred into a thermal evaporator where the organic small molecule semiconductor was evaporated under high vacuum (~10⁻⁵ Pa) onto the substrate to achieve 30 nm thickness monitored using quartz. The fabricated OFET was then transferred into a vacuum chamber (~10⁻³ Pa) and the device performance was measured using a Keithley 4200A-SCS parameter analyser. The mobility (μ) in the linear regime was calculated from the drain current and the gate voltage fitted into the equation:

$$\mu = \frac{d}{\epsilon_0 \epsilon_r} \times \frac{L}{W} \times \frac{dI_D}{dV_G}$$

where *d* is the thickness of SiO₂ (350 nm), ε₀ is the vacuum permittivity of electric constant (8.854 × 10⁻¹² F m⁻¹), ε_r is the relative permittivity of silicon dioxide (3.9), *L* is the gap electrode length, and *W* is the width of the electrode.

Synthesis of T-NT-T, F-NT-F, T-BT-T and F-BT-F

Compounds 5–8 (130 mg, 0.30 mmol), 5-hexyl-2-thiophene boronic acid pinacol ester (225 mg, 0.76 mmol), Pd(PPh₃)₄ (20 mg, 0.02 mmol), and 2 M Na₂CO₃ (5.4 mL) were added into a 100 mL round-bottom flask. THF (15 mL) was added as a solvent and then the mixture was stirred and degassed with N₂ for 5 min. The mixture was stirred at reflux under N₂ for 24 h. After cooling, the mixture was extracted with dichloromethane (70 mL × 2). The combined organic phase was washed with water (70 mL) and brine solution (70 mL), dried over anhydrous Na₂SO₄, filtered and evaporated to dryness. To obtain a product of higher purity, the residue was further purified by silica column chromatography eluting with the mixture of dichloromethane and hexane (1 : 3) followed by recrystallisation from the mixed solvent of dichloromethane and methanol.

F-BT-F. Dark pink solids (87%). ¹H NMR (600 MHz, CDCl₃) δ ppm: 8.07 (s, 2H), 7.72 (s, 2H), 7.21 (s, 2H), 6.76 (d, *J* = 3.36, 2H), 6.64 (d, *J* = 2.46 Hz, 2H), 2.84 (s, 4H), 1.72 (m, 4H), 1.41 (m, 4H), 1.33 (m, 8H), 0.90 (t, *J* = 6.72, 6H); ¹³C NMR (151 MHz, CDCl₃) δ 151.41, 150.03, 148.99, 146.11, 130.92, 124.94, 123.07, 121.09, 114.62, 107.45, 31.62, 31.67, 30.25, 28.84, 22.65, 14.15; HRMS MALDI-TOF *m/z* [M]⁺: calcd for C₃₆H₃₆N₂O₂S₃ 600.1939; found 600.4812.

T-BT-T. Dark red solids (84%). ¹H NMR (600 MHz, CDCl₃) δ ppm: 8.03 (d, *J* = 3.78 Hz, 2H), 7.80 (s, 2H), 7.18 (d, *J* = 3.84 Hz, 2H), 7.10 (d, *J* = 3.42 Hz, 2H), 6.72 (d, *J* = 3.48 Hz, 2H), 2.81 (t, *J* = 7.56 Hz, 4H), 1.70 (m, 4H), 1.40 (m, 4H), 1.33 (m, 8H), 0.90 (t, *J* = 6.90 Hz, 6H); ¹³C NMR (151 MHz, CDCl₃) δ 152.53, 146.07, 139.41, 137.46, 134.65, 128.27, 125.53, 125.10, 124.97, 123.83, 123.79, 31.58, 30.25, 28.78, 22.58, 14.06; HRMS MALDI-TOF *m/z* [M]⁺: calcd for C₃₄H₃₆N₂S₅ 632.1482; found 632.4111.

F-NT-F. Dark blue solids (65%). ¹H NMR (600 MHz, CD₃COCD₃) δ ppm: 8.90 (dd, *J* = 7.02 Hz, 3.12 Hz, 2H), 7.65 (d, *J* = 3.36, 2H), 7.60 (dd, *J* = 7.14 Hz, 3.06 Hz, 2H), 7.34 (d, *J* = 3.42 Hz, 2H), 6.96 (d, *J* = 3.36 Hz, 2H), 6.89 (d, *J* = 3.18 Hz, 2H), 2.88 (t, *J* = 7.44 Hz, 4H), 1.73 (m, 4H), 1.44 (s, 4H), 1.34 (t, *J* = 3.36 Hz, 8H), 0.89 (t, *J* = 6.66 Hz, 6H); ¹³C NMR (151 MHz, CD₃COCD₃) δ 150.71, 150.25, 149.01, 146.08, 130.86, 130.65, 127.40, 127.19, 125.42, 124.96, 123.45, 122.62, 118.37, 106.98, 31.52, 31.46, 31.36, 22.32, 13.39; HRMS MALDI-TOF *m/z* [M]⁺: calcd for C₃₈H₃₈N₂O₂S₃ 650.2095; found 650.5062.

T-NT-T. Purple solids (66%). ¹H NMR (600 MHz, CDCl₃) δ ppm: 8.44 (dd, *J* = 6.72 Hz, 2.88 Hz, 2H), 7.45 (dd, *J* = 6.90 Hz, 2.82 Hz, 2H), 7.39 (d, *J* = 2.40 Hz, 2H), 7.31 (d, *J* = 3.36 Hz, 2H), 7.11 (d, *J* = 2.46 Hz, 2H), 6.73 (d, *J* = 2.46 Hz, 2H), 2.83 (t, *J* = 7.32 Hz, 4H), 1.71 (m, 4H), 1.41 (s, 4H), 1.33 (t, *J* = 3.42, 8H), 0.90 (t, *J* = 6.30 Hz, 6H); ¹³C NMR (151 MHz, CDCl₃) δ 151.50, 146.03, 140.81, 134.64, 134.39, 132.84, 131.37, 127.09, 127.03, 124.91, 123.88, 123.19, 123.14, 31.58, 31.56, 30.25, 28.76, 22.58, 14.08; HRMS MALDI-TOF *m/z* [M]⁺: calcd for C₃₈H₃₈N₂S₅ 682.1639; found 682.4468.

Conflicts of interest

There are no conflicts to declare.

Acknowledgements

This research work was financially supported by the Thailand Research Fund (RTA6080005); the Grant-in-Aid for Scientific Research (A) (No. 19H00891) from the Japan Society for the Promotion of Science (JSPS); and the National Nanotechnology Center, National Science and Technology Development Agency, Ministry of Higher Education, Science, Research and Innovation, Thailand, through its program of Research Network National Nanotechnology Center. Part of this work was conducted at the Equipment Development Center (Institute for Molecular Science) supported by the Nanotechnology Platform Program of the Ministry of Education, Culture, Sport, Science and Technology (MEXT), Japan. Thanks also go to Vidyasirimedhi Institute of Science and Technology for the support of both the PhD research grant and equipment.

References

- (a) B. Kumar, B. K. Kaushik and Y. S. Negi, *Polym. Rev.*, 2014, **54**, 33–111; (b) B. McDearmon, Z. A. Page, M. L. Chabinyc and C. J. Hawker, *J. Mater. Chem. C*, 2018, **6**, 3564–3572; (c) F. G. Brunetti, R. Kumar and F. Wudl, *J. Mater. Chem.*, 2010, **20**, 2934–2948.
- (a) R. Ilmi, A. Haque and M. S. Khan, *Org. Electron.*, 2018, **58**, 53–62; (b) T. T. Do, Y. Takeda, S. Manzhos, J. Bell, S. Tokito and P. Sonar, *J. Mater. Chem. C*, 2018, **6**, 3774–3786; (c) W. C. Chen, Y. Yuan, Z. L. Zhu, Z. Q. Jiang, L. S. Liao and C. S. Lee, *Adv. Opt. Mater.*, 2018, **6**, 1–9.
- (a) W. Wu, Y. Liu and D. Zhu, *Chem. Soc. Rev.*, 2010, **39**, 1489–1502; (b) S. R. Forrest, *Nature*, 2004, **428**, 911–918; (c) C. Liu, Y. Xu and Y. Y. Noh, *Mater. Today*, 2015, **18**, 79–96.
- H. Sirringhaus, *Adv. Mater.*, 2014, **26**, 1319–1335.
- (a) W. Tang, Y. Huang, L. Han, R. Liu, Y. Su, X. Guo and F. Yan, *J. Mater. Chem. C*, 2019, **7**, 790–808; (b) L. Zhang, C. A. Di, G. Yu and Y. Liu, *J. Mater. Chem.*, 2010, **20**, 7059–7073.
- (a) W. Li, K. H. Hendriks, W. S. C. Roelofs, Y. Kim, M. M. Wienk and R. A. J. Janssen, *Adv. Mater.*, 2013, **25**, 3182–3186; (b) S. H. Kang, W. S. Hwang, Z. Lin, S. H. Kwon and S. W. Hong, *Nano Lett.*, 2015, **15**, 7913–7920.
- (a) A. L. Briseno, R. J. Tseng, M. M. Ling, E. H. L. Falcao, Y. Yang, F. Wudl and Z. Bao, *Adv. Mater.*, 2006, **18**, 2320–2324; (b) B. Lim, H. Sun, J. Lee and Y. Y. Noh, *Sci. Rep.*, 2017, **7**, 1–8.
- (a) M. J. Kim, Y. Seul Lee, S. Chul Shin and Y. H. Kim, *J. Polym. Sci., Part A: Polym. Chem.*, 2016, **54**, 525–531; (b) J. W. Rumer, M. Levick, S. Y. Dai, R. Stephan, Z. Huang, B. Laure, T. D. Anthopoulos, J. R. Durrant, D. J. Procter and I. Mc Culloch, *Chem. Commun.*, 2013, **49**, 4565–4567; (c) H. Hu, K. Jiang, J. H. Kim, G. Yang, Z. Li, T. Ma, G. Lu, Y. Qu, H. Ade and H. Yan, *J. Mater. Chem. A*, 2016, **4**, 5039–5043.
- (a) Y. Liang, Y. Wu, D. Feng, S. T. Tsai, H. J. Son, G. Li and L. Yu, *J. Am. Chem. Soc.*, 2009, **131**, 56–57; (b) S. J. Lou, J. M. Szarko, T. Xu, L. Yu, T. J. Marks and L. X. Chen, *J. Am. Chem. Soc.*, 2011, **133**, 20661–20663; (c) H. Li, P. Jiang, C. Yi, C. Li, S. X. Liu, S. Tan, B. Zhao, J. Braun, W. Meier, T. Wandlowski and S. Decurtins, *Macromolecules*, 2010, **43**, 8058–8062.

- 10 (a) H. Dong, X. Fu, J. Liu, Z. Wang and W. Hu, *Adv. Mater.*, 2013, **25**, 6158–6183; (b) S. Holliday, J. E. Donaghey and I. McCulloch, *Chem. Mater.*, 2014, **26**, 647–663; (c) H. N. Tsao, D. M. Cho, I. Park, M. R. Hansen, A. Mavrinskiy, D. Y. Yoon, R. Graf, W. Pisula, H. W. Spiess and K. Müllen, *J. Am. Chem. Soc.*, 2011, **133**, 2605–2612.
- 11 K. Takimiya, Y. Kunugi, Y. Konda, N. Niihara and T. Otsubo, *J. Am. Chem. Soc.*, 2004, **126**, 5084–5085.
- 12 (a) P. Sonar, S. P. Singh, Y. Li, M. S. Soh and A. Dodabalapur, *Adv. Mater.*, 2010, **22**, 5409–5413; (b) Z. Chen, H. Lemke, S. Albert-Seifried, M. Caironi, M. M. Nielsen, M. Heeney, W. Zhang, I. McCulloch and H. Sirringhaus, *Adv. Mater.*, 2010, **22**, 2371–2375; (c) Z. Chen, M. J. Lee, R. Shahid Ashraf, Y. Gu, S. Albert-Seifried, M. Meedom Nielsen, B. Schroeder, T. D. Anthopoulos, M. Heeney, I. McCulloch and H. Sirringhaus, *Adv. Mater.*, 2012, **24**, 647–652; (d) J. D. Yuen, J. Fan, J. Seifert, B. Lim, R. Hufschmid, A. J. Heeger and F. Wudl, *J. Am. Chem. Soc.*, 2011, **133**, 20799–20807.
- 13 H. Limpricht, *Ber. Dtsch. Chem. Ges.*, 1870, **3**, 90–91.
- 14 Z. Zhao, H. Nie, C. Ge, Y. Cai, Y. Xiong, J. Qi, W. Wu, R. T. K. Kwok, X. Gao, A. Qin, J. W. Y. Lam and B. Z. Tang, *Adv. Sci.*, 2017, **4**, 1–8.
- 15 (a) M. Okada, K. Tachikawa and K. Aoi, *J. Appl. Polym. Sci.*, 1999, **74**, 3342–3350; (b) F. Koopman, N. Wierckx, J. H. De Winde and H. J. Ruijsenaars, *Proc. Natl. Acad. Sci. U. S. A.*, 2010, **107**, 4919–4924; (c) A. Gandini, *ACS Symp. Ser.*, 1990, **433**, 195–208.
- 16 (a) O. Gidron, A. Dadvand, Y. Sheynin, M. Bendikov and D. F. Perepichka, *Chem. Commun.*, 2011, **47**, 1976–1978; (b) B. Walker, A. B. Tamayo, X. D. Dang, P. Zalar, J. H. Seo, A. Garcia, M. Tantiwiwat and T. Q. Nguyen, *Adv. Funct. Mater.*, 2009, **19**, 3063–3069; (c) J. C. Bijleveld, B. P. Karsten, S. G. J. Mathijssen, M. M. Wienk, D. M. De Leeuw and R. A. J. Janssen, *J. Mater. Chem.*, 2011, **21**, 1600–1606.
- 17 (a) S. M. Lee, H. R. Lee, G. K. Dutta, J. Lee, J. H. Oh and C. Yang, *Polym. Chem.*, 2019, **10**, 2854–2862; (b) S. M. Lee, H. R. Lee, A. R. Han, J. Lee, J. H. Oh and C. Yang, *ACS Appl. Mater. Interfaces*, 2017, **9**, 15652–15661; (c) Z. Cai, Y. Guo, S. Yang, Q. Peng, H. Luo, Z. Liu, G. Zhang, Y. Liu and D. Zhang, *Chem. Mater.*, 2013, **25**, 471–478.
- 18 (a) C. Bulumulla, R. Gunawardhana, R. N. Kularatne, M. E. Hill, G. T. McCandless, M. C. Biewer and M. C. Stefan, *ACS Appl. Mater. Interfaces*, 2018, **10**, 11818–11825; (b) C. Bulumulla, R. Gunawardhana, S. H. Yoo, C. R. Mills, R. N. Kularatne, T. N. Jackson, M. C. Biewer, E. D. Gomez and M. C. Stefan, *J. Mater. Chem. C*, 2018, **6**, 10050–10058; (c) T. Minari, Y. Miyata, M. Terayama, T. Nemoto, T. Nishinaga, K. Komatsu and S. Isod, *Appl. Phys. Lett.*, 2006, **88**, 083415.
- 19 P. Sonar, S. P. Singh, S. Sudhakar, A. Dodabalapur and A. Sellinger, *Chem. Mater.*, 2008, **20**, 3184–3190.
- 20 C. B. Nielsen, M. Turbiez and I. McCulloch, *Adv. Mater.*, 2013, **25**, 1859–1880.
- 21 Y. Zhang, X. Cai, D. Qi, Y. Bian and J. Jiang, *J. Phys. Chem. C*, 2008, **112**, 14579–14588.
- 22 (a) D. Raychev, O. Guskova, G. Seifert and J. U. Sommer, *Comput. Mater. Sci.*, 2017, **126**, 287–298; (b) N. E. Jackson, B. M. Savoie, K. L. Kohlstedt, M. Olvera De La Cruz, G. C. Schatz, L. X. Chen and M. A. Ratner, *J. Am. Chem. Soc.*, 2013, **135**, 10475–10483; (c) H. Kayi, *J. Mol. Model.*, 2014, **20**, 1–7.
- 23 I. Kymissis, *Organic Field Effect Transistors, Theory, Fabrication and Characterization*, Springer, US, 2009.
- 24 (a) M. Devynck, P. Tardy, G. Wantz, Y. Nicolas and L. Hirsch, *EPJ Appl. Phys.*, 2011, **56**, 34106; (b) S. Sinha, C. H. Wang and M. Mukherjee, *Thin Solid Films*, 2017, **638**, 167–172; (c) M. Robin, M. Harnois, Y. Molard and E. Jacques, *Org. Electron.*, 2016, **39**, 214–221.
- 25 (a) Y. Don Park, J. A. Lim, H. S. Lee and K. Cho, *Mater. Today*, 2007, **10**, 46–54; (b) H. I. Un, J. Y. Wang and J. Pei, *Adv. Sci.*, 2019, **6**, 1900375; (c) M. S. Chen, J. R. Niskala, D. A. Unruh, C. K. Chu, O. P. Lee and J. M. J. Fréchet, *Chem. Mater.*, 2013, **25**, 4088–4096.
- 26 (a) A. L. Spek, *J. Appl. Crystallogr.*, 2003, **36**, 7–13; (b) A. L. Spek, *Acta Crystallogr., Sect. D: Biol. Crystallogr.*, 2009, **65**, 148–155; (c) A. L. Spek, *Acta Crystallogr., Sect. E: Crystallogr. Commun.*, 2020, **76**, 1–11.
- 27 M. J. Frisch, G. W. Trucks, H. B. Schlegel, G. E. Scuseria, M. A. Robb, J. R. Cheeseman, G. Scalmani, V. Barone, B. Mennucci, G. A. Petersson, H. Nakatsuji, M. Caricato, X. Li, H. P. Hratchian, A. F. Izmaylov, J. Bloino, G. Zheng, J. L. Sonnenberg, M. Hada, M. Ehara, K. Toyota, R. Fukuda, J. Hasegawa, M. Ishida, T. Nakajima, Y. Honda, O. Kitao, H. Nakai, T. Vreven, J. A. Montgomery Jr, J. E. Peralta, F. Ogliaro, M. Bearpark, J. J. Heyd, E. Brothers, K. N. Kudin, V. N. Staroverov, R. Kobayashi, J. Normand, K. Raghavachari, A. Rendell, J. C. Burant, S. S. Iyengar, J. Tomasi, M. Cossi, N. Rega, J. M. Millam, M. Klene, J. E. Knox, J. B. Cross, V. Bakken, C. Adamo, J. Jaramillo, R. Gomperts, R. E. Stratmann, O. Yazyev, A. J. Austin, R. Cammi, C. Pomelli, J. W. Ochterski, R. L. Martin, K. Morokuma, V. G. Zakrzewski, G. A. Voth, P. Salvador, J. J. Dannenberg, S. Dapprich, A. D. Daniels, O. Farkas, J. B. Foresman, J. V. Ortiz, J. Cioslowski and D. J. Fox, *Gaussian 09*, Gaussian, Inc., Wallingford CT, 2009.